

Nonlinear Evolution of the Magnetorotational Instability in Ion-Neutral Disks

John F. Hawley

Department of Astronomy, University of Virginia,
Charlottesville, VA 22903; jh8h@virginia.edu

James M. Stone

Department of Astronomy, University of Maryland,
College Park, MD 20742; jstone@astro.umd.edu

Received _____; accepted _____

ABSTRACT

We carry out three-dimensional magnetohydrodynamical simulations of the magnetorotational (Balbus-Hawley) instability in weakly-ionized plasmas. We adopt a formulation in which the ions and neutrals each are treated as separate fluids coupled only through a collisional drag term. Ionization and recombination processes are not considered. The linear stability of the ion-neutral system has been previously considered by Blaes & Balbus (1994). Here we extend their results into the nonlinear regime by computing the evolution of Keplerian angular momentum distribution in the local shearing box approximation. We find significant turbulence and angular momentum transport when the collisional frequency is on order 100 times the orbital frequency Ω . At higher collision rates, the two-fluid system studied here behaves much like the fully ionized systems studied previously. At lower collision rates the evolution of the instability is determined primarily by the properties of the ions, with the neutrals acting as a sink for the turbulence. Since in this regime saturation occurs when the magnetic field is superthermal with respect to the ion pressure, we find the amplitude of the magnetic energy and the corresponding angular momentum transport rate is proportional to the ion density. Our calculations show the ions and neutrals are essentially decoupled when the collision frequency is less than 0.01Ω ; in this case the ion fluid behaves as in the single fluid simulations and the neutrals remain quiescent. We find that purely toroidal initial magnetic field configurations are unstable to the magnetorotational instability across the range of coupling frequencies.

Subject headings: accretion, accretion disks–protostellar disks–instabilities–MHD

1. Introduction

The key to understanding accretion disk dynamics lies with the angular momentum transport mechanism. Since the molecular viscosity of disks is very low, some form of “anomalous viscosity” must be present. Although the precise nature of this anomalous viscosity has long been elusive, the discovery that differentially rotating systems are magnetohydrodynamically (MHD) unstable (Balbus & Hawley 1991) has led to the conclusion that fully ionized disks must be MHD turbulent. Because this magnetorotational instability is caused by angular momentum transport, the resulting turbulence has precisely the right character to transport angular momentum outwards (Balbus, Hawley & Stone 1996, hereafter BHS96), as required for disks to accrete. Since the MHD instability plays such a fundamental role in disks, the question naturally arises, what is its behavior when the plasma is not fully ionized? Protostellar and protoplanetary disks as well as other molecular disks are the venues where this question is particularly significant.

Although it is tempting to assume that in the absence of MHD turbulence, purely hydrodynamical turbulence will rise to the task of transporting angular momentum, this now seems highly unlikely. BHS96 demonstrated, through a combination of analysis and simulation, that differentially rotating systems are both linearly and nonlinearly locally stable to hydrodynamic perturbations so long as the standard Rayleigh criterion is satisfied. Even if initiated “by hand,” hydrodynamic turbulence is not self-sustaining. Outward transport of angular momentum through a net Reynolds stress requires a specific average correlation between the radial velocity and the angular momentum fluctuations in the turbulent flow. Of fundamental importance is the interaction of these velocity fluctuations with the background mean flow. In differentially rotating systems the source of free energy is the angular velocity gradient. Angular momentum fluctuations, on the other hand, act to reduce the background angular *momentum* gradient, which has the opposite sign from the angular velocity gradient. A positive value of the Reynolds stress, required to tap into the free energy of the system, acts as a sink term for the evolution of the angular velocity fluctuations that make up the Reynolds stress itself. Thus the turbulence is not self-sustaining.

The results of BHS96 further imply that enhanced angular momentum transport is not the necessary outcome of turbulence. Because transport requires a high degree of correlation between the radial and azimuthal velocity fluctuations, turbulence that does not have its origin in the mean differentially rotating flow is unlikely to be an efficient source of angular momentum transport. This point is emphasized by Stone & Balbus (1996), whose numerical simulation showed that while vertical convection can generate turbulence, the resulting net radial angular momentum transport was *inward* at a low rate (so long as the equator was kept hot by the boundary conditions of the simulation). Similar results were found by Cabot (1996). Simulations by Ryu & Goodman (1994) of the action of a parametric tidal instability on a disk show the generation of turbulence, but without internal transport. These studies provide compelling evidence that the idea of purely hydrodynamic turbulence as an *angular momentum transport mechanism* in protostellar disks should be discarded. If turbulence is to be driven by the differential rotation, it must be MHD turbulence. If hydrodynamic turbulence is present, it must be driven by some source other than the background shear and generally will not transport angular momentum. Such considerations are particularly important if turbulence is important in protoplanetary disks for chondrule and planetesimal formation (e.g., Cuzzi, Dobrovolskis & Hogan 1996).

It now appears that the number of different mechanisms for transporting angular

momentum in disks is very limited. Magnetic fields and spiral wave disturbances (nonaxisymmetric distortions) are the only viable general mechanisms. In the latter category, and within the context of protostellar disks, nonaxisymmetric gravitational instabilities may be important. Global wave mechanisms, however, are not normally associated with the generation of local turbulence. The dynamics of a disk controlled by such global waves will be quite different from a model based upon the usual local α prescription for viscosity, which is itself based upon the ansatz of transport by local turbulent stresses.

For protostellar disks we are forced to reckon with questions of the effectiveness of magnetic field coupling. There is, of course, nothing about this issue that is unique to the magnetorotational instability. If the magnetic field is not well coupled to the fluid, then all potential MHD processes in the disk will be affected. It is difficult to imagine, for example, a scenario in which a weak field in a disk is stabilized by low ion-neutral coupling, yet remains involved in, say, a kinematic dynamo. If a protostellar disk or rotating molecular cloud is sufficiently well-coupled to a weak magnetic field for the field to be important in any way, then the magnetorotational instability is an important dynamical factor.

Under what circumstances, then, will the instability operate and produce MHD turbulence in protoplanetary disks where the ionization fraction is quite low? The first step towards answering this question was taken by Blaes & Balbus (1994, hereafter BB), who performed an axisymmetric linear stability analysis for a vertical (and toroidal) field in a weakly ionized plasma for a number of limits. Their major finding is that the linear magnetorotational instability is present so long as the ion-neutral collision frequency exceeds the local epicyclic frequency. This condition will be satisfied even for very small ionization fractions. They also found that azimuthal fields can reduce the observed growth rates, although such fields do not eliminate the instability.

While a linear analysis can indicate the presence or absence of the instability, its effectiveness as a transport mechanism must be determined by its nonlinear evolution. The first numerical study of the two-fluid magnetorotational instability was carried out by Mac Low et al. (1995). They assume ionization-recombination equilibrium and consider the low-ionization limit, neglecting the ion pressure and inertia. This reduces the problem to a single-fluid (neutral) plus a diffusion term in the induction equation (ambipolar diffusion limit). Using the ZEUS code they carried out a series of two-dimensional simulations of the vertical flux tube problem (as in Hawley & Balbus 1991) for various ion-neutral coupling strengths. Although these simulations did not follow the evolution much beyond the linear stage, the results were in agreement with the stability analysis of BB in the appropriate limit. Essentially, so long as there are unstable wavelengths available, and the coupling between ions and neutrals is sufficiently strong, the instability behaves much like the single fluid case. The instability ceases to operate when the ambipolar diffusion rate becomes comparable to the growth rate of the instability, i.e., the field diffusion time is $< \Omega^{-1}$, where Ω is the disk orbital frequency.

In another study, Brandenburg et al. (1995) investigated the ambipolar diffusion limit in three-dimensional simulations of a local, vertically stratified disk. They considered a case where the ambipolar diffusion time was long compared to the orbital time. They found that in this limit (i.e., ambipolar diffusion sufficiently small) the instability remains effective, and continues to generate self-sustained turbulence that transports angular momentum outward, albeit at a rate slightly reduced from the fully-coupled case. In another simulation, the diffusion time was set comparable to Ω^{-1} and the turbulence decayed.

These first results, while important, are only a beginning. To date, all the numerical studies have considered the behavior of the partially ionized system in the limit where the inertia of the ions can be completely neglected, and where the ion density is everywhere a fixed power-law function of the neutral density. In this paper we will approach the problem using a genuine two-fluid, ion-neutral evolution to examine effects where the ions are free to move relative to the neutrals. We will investigate the transition from the well-coupled regime, through critical coupling where the collision frequency is comparable to the epicyclic frequency, and down to the fully uncoupled limit. This parameter study should more clearly define the physical conditions for which full MHD turbulence and accompanying angular momentum transport can be expected, and those for which the bulk of the system dynamics are essentially hydrodynamic. The full range of conditions is likely to be of importance somewhere within protostellar or protoplanetary disks. In some regions of these disk systems, the ionization fractions may be quite small, but in other regions, such as near the forming protostar, the temperatures will be high, and the gas will be nearly fully ionized. In between, there will be a transition region. Determining the size of this transition region, and delineating its properties, will depend on obtaining a better understanding of the nonlinear behavior of the ion-neutral system in various regimes.

The plan of the paper is as follows. In §2 we will consider the equations and the numerical techniques used to solve them. Although the collision term is handled semi-implicitly, the use of explicit finite-differencing for the remainder of the system makes the code Courant-limited. As a test problem, we compare numerical growth rates with analytic values from BB. In §3 we present the results of an extensive ensemble of simulations, covering a range of ionization fractions and coupling frequencies. Because of the Courant limit, this study is limited to relatively large ionization fractions $f \equiv \rho_i/(\rho_i + \rho_n)$. In the linear limit, however, the growth rates for small ionization fractions are relatively unaffected by decreasing f , if the ratio of the coupling frequency to orbital frequency is held constant. Thus, we expect that physical insights gained by this study should extend even into the small f regime. The implications of the simulations will be summarized and discussed in §4.

2. Two-Fluid Algorithm

2.1. Equations and Numerics

In these simulations we will be studying the simple two-fluid system as described in §3 of BB, consisting of separate compressible ion and neutral fluids, coupled only by collisions. The ion fluid is assumed to be perfectly conducting. We include no ionization or recombination; ions and neutrals are separately conserved. We have examined both isothermal systems, and ones where the two fluids can have different temperatures and no thermal coupling is included.

As in previous work (Hawley, Gammie & Balbus 1995, hereafter HGB95) we restrict our attention to the local Hill (1878) system representation of a disk. This model incorporates Coriolis and tidal forces, and is constructed by expanding the equations of motion in

cylindrical coordinates (R, ϕ, z) to first order around a fiducial radius R_o using a set of local Cartesian coordinates $\mathbf{x} = (x, y, z) = (R - R_o, R_o[\phi - \Omega t], z)$. The rotation law is assumed to have the form $\Omega \sim R^{-q}$; for a Keplerian disk $q = 3/2$. The resulting equations for the ions, neutrals, and magnetic field are

$$\frac{\partial \rho_i}{\partial t} + \nabla \cdot (\rho_i \mathbf{v}_i) = 0, \quad (1)$$

$$\frac{\partial \rho_n}{\partial t} + \nabla \cdot (\rho_n \mathbf{v}_n) = 0, \quad (2)$$

$$\frac{\partial \mathbf{v}_i}{\partial t} + \mathbf{v}_i \cdot \nabla \mathbf{v}_i = -\frac{1}{\rho_i} \nabla \left(P_i + \frac{B^2}{8\pi} \right) + \frac{(\mathbf{B} \cdot \nabla) \mathbf{B}}{4\pi \rho_i} - 2\boldsymbol{\Omega} \times \mathbf{v}_i + 2q\Omega^2 x \hat{\mathbf{x}} + \gamma \rho_n (\mathbf{v}_n - \mathbf{v}_i), \quad (3)$$

$$\frac{\partial \mathbf{v}_n}{\partial t} + \mathbf{v}_n \cdot \nabla \mathbf{v}_n = -\frac{1}{\rho_n} \nabla P_n - 2\boldsymbol{\Omega} \times \mathbf{v}_n + 2q\Omega^2 x \hat{\mathbf{x}} - \gamma \rho_i (\mathbf{v}_n - \mathbf{v}_i), \quad (4)$$

$$\frac{\partial \mathbf{B}}{\partial t} = \nabla \times (\mathbf{v}_i \times \mathbf{B}), \quad (5)$$

where the terms have their usual meaning, the subscripts n and i refer to the neutrals and ions respectively, and γ is the drag coefficient due to collisions between the two fluids. In addition, there is an equation of state (we use either an adiabatic or an isothermal equation of state) for the neutrals and for the ions. In these equations we neglect vertical gravity and assume that the ion component is a perfectly conducting fluid. While there are physically important regimes where resistivity will be important (see, e.g., the discussion in BB), we make this assumption to simplify the parameters of the present study. The results of this paper will correspond to the most favorable conditions for the MHD instability since finite resistivity would be expected to reduce the levels of the resulting turbulence.

Equations (1)–(5) amount to separate hydrodynamical (neutrals) and MHD (ions) systems, coupled by the collisional drag term. We use the hydrodynamical algorithms described by Stone & Norman (1992a) to evolve the equations for the neutrals (eqs. [1–2] and [4]), and the MOCCT algorithm (Stone & Norman 1992b; Hawley & Stone 1995) to evolve the ions (eqs. [3] and [5]). The collisional drag term γ in both equations (3) and (4) is operator-split and updated using fully implicit backward Euler differencing (a complete description of the resulting difference equations is given in Stone 1997). This avoids the Courant stability criterion associated with diffusion of the magnetic field that restricts explicit differencing formalisms of the drag term. The resulting hybrid hydrodynamical-MHD code has been tested with steady C-type shock solutions and comparison to the analytic growth rate of the Wardle instability (Stone 1997). We describe a comparison of the numerical growth rate of the magnetorotational instability in a partially ionized disk with the analytic value from BB in §2.2 below.

The computations are done in the periodic three-dimensional (3D) shearing box (HGB95). In this system the computational domain is a rectangular box with sides L_x, L_y , and L_z , and it is assumed to be surrounded by identical boxes that are strictly periodic at $t = 0$. A large-scale continuous linear shear flow is present across all the boxes. At later times the computational box remains periodic in y and z , while the radial (x) boundary condition is determined by the location of the neighboring boxes as they move relative to one another due to the background shear. We use box dimensions of $L_x = 1$, $L_y = 2\pi$, and $L_z = 1$, as in previous single-fluid simulations (HGB95).

The initial equilibrium system has a Keplerian rotation law ($q = 3/2$); the angular speed at the center of the shearing box is Ω . The initial state has constant densities and pressures (ion and neutral). For most experiments we use an isothermal equation of state; in a few simulations we use of an adiabatic equation of state with $P \propto \rho^{5/3}$. The mean molecular weight of the ions and the neutrals can be specified separately; for most simulations we adopt the weights used in BB, $m_n = 2.33m_H$ and $m_i = 30m_H$. These numbers come from assuming that the neutrals are hydrogen and helium molecules while the ions correspond to trace alkali species (Draine, Roberge, & Dalgarno 1983). Assuming thermal equilibrium, the ratio of the initial sound speeds in the neutrals and ions is equal to the square root of the ratio of the mean molecular weights.

One of the difficulties of this study is the wide range of possible physical parameters that could be investigated. Among these are the equation of state, neutral to ion mass ratio, initial field strength and orientation, the initial ionization fraction $f \equiv \rho_i/(\rho_i + \rho_n)$, and the collisional frequency, $\rho_i\gamma/\Omega$. Our primary focus will be on the role of the collisional drag term γ . In the limit of $\gamma \rightarrow 0$, the ion and neutral fluids decouple; the ions evolve as in the magnetized single-fluid case, while the neutrals evolve hydrodynamically. In the other extreme, $\gamma \rightarrow \infty$, the system reduces to a single well-coupled fluid. In this study, we will examine a range of collisional frequencies on either side of the critical frequency, $\gamma\rho_i \sim \Omega$, by treating γ as a free parameter and varying it for given values of ionization fraction and Ω . The Courant condition from the ion Alfvén speed limits the simulations to moderate values of the ionization fraction $f \geq 0.001$. As BB have shown, it is the ratio of the collisional frequency to the orbital frequency that determines the linear behavior of the instability. Assuming this holds even into the nonlinear regime, our results should be able to set important limits even for significantly smaller, and hence more realistic, ionization fractions.

2.2. Two-Dimensional Test Simulation

As a simple verification test of the two-fluid code, we compare observed growth rates in the linear regime of the instability with analytic values from BB. (Similar tests were performed for the fully-coupled, single-fluid system by Hawley and Balbus 1992.) We choose an initial magnetic field strength corresponding to $\beta_i = P_{ion}/P_{mag} = 2$, run several models with $f = 0.1$ and different values γ , and compare the observed growth rate in the perturbed magnetic radial field B_x with the value given by the dispersion relation (BB eq. [25]) for the largest vertical wavelength permitted by the computational domain. The particular initial magnetic field strength used makes the (analytically determined) fastest growing wavelength close to the domain size $L_z = 1$. We use two resolutions, 63×63 and 31×31 grid zones; these are the (x, z) resolutions that will be used in the 3D simulations to follow. The numerical growth rates, in units of Ω , are plotted on top of an analytic growth rate curve obtained from equation (24) of BB (Fig. 1). As can be seen from the figure, the two-fluid code reproduces the analytic linear growth rates for the range of collision frequencies considered. There is not much difference between the high and low resolution simulations; the long wavelength modes considered here are adequately resolved by either grid.

3. Results

3.1. A Review of Single Fluid Results

In this paper our primary focus will be on an initially uniform vertical magnetic field, B_z . The single-fluid, fully-ionized version of this problem was investigated by HGB95, and we begin with a brief summary of their results.

The maximum growth rate of the single-fluid system is 0.75Ω . HGB95 found this growth rate for wavenumbers $kv_{Az}/\Omega \simeq 1$ in all simulations where the fastest growing wavelength is adequately resolved on the grid. The fastest growing mode is axisymmetric and leads to flow along radial “channels.” Outward flowing channels contain excess angular momentum, while inward flowing channels have less than the Keplerian value. When the fastest growing mode has a vertical wavelength greater than or equal to the radial dimension of the box, this axisymmetric mode continues to grow exponentially well into the strong field regime. However, for smaller vertical wavelengths (larger vertical wavenumbers), the channels break down into turbulence. These numerical results can be understood through the analysis of Goodman & Xu (1994) who found that, in the local limit and for a uniform vertical field, the exponentially-growing linear solution is also an exact *nonlinear* solution. Goodman & Xu further carried out a stability analysis of the streaming channel solution and found that it was subject to a number of instabilities. The most important of these parasitic instabilities is a magnetized Kelvin-Helmholtz mode that is present for radial wavelengths larger than the channel solution’s vertical wavelength. Thus, under most circumstances, the channel solution is unstable, and the general outcome of the instability is turbulence.

The resulting turbulence is nonisotropic; correlated fluctuations in the magnetic and velocity fields transfer angular momentum outward through the action of the Maxwell (magnetic) and the Reynolds stresses. Accretion disk models often make use of the Shakura & Sunyaev (1973) parameterization for the stress $W_{r\phi}$, scaling it with the total pressure, $W_{r\phi} = \alpha P$. In the MHD turbulence, however, the level of net transport depends primarily upon the magnetic field levels in the saturated turbulent state. The stress is proportional to the *magnetic* pressure with a ratio of the stress to P_{mag} of about 0.6. We refer to this ratio as α_{mag} .

The complete ensemble of HGB95 vertical field simulations provides an empirical relation for the average magnetic field energy in the turbulence: it is proportional to the product of the fastest growing initial wavelength and the maximum possible unstable wavelength permitted in the computational domain. From HGB95, we have

$$\left\langle \frac{B^2}{8\pi} \right\rangle \propto \rho(L_z\Omega)(\lambda_c\Omega), \quad (6)$$

where λ_c is the fastest growing wavelength for the initial magnetic field ($\lambda_c = 2\pi[16/15]^{1/2}v_A/\Omega$). A best fit to the HGB95 simulations gives a constant of proportionality of 1.2. In essence, the final energy is the geometric average of the energy of the *net* vertical field piercing the box (which, because of the periodic boundary conditions does not change as a result of the evolution) and the energy of the largest magnetic field

that would be unstable given the dimension L_z . The box dimension L_z was set equal to c_s/Ω to represent a disk scale height, although vertical gravity was not included in these simulations. The growth of the instability and its saturation level are unaffected by the hydrodynamic pressure in the box; the magnetic field energy remains subthermal (since the dimensions of the computational domain were chosen so that the sound speed was equal to $L_z\Omega$.) The saturation amplitude is also unaffected by the presence of a subthermal toroidal field except to the extent that such a toroidal field and its instabilities add to the total magnetic energy.

3.2. Two-fluid system: uniform B_z fields

We now turn to the two-fluid system and begin with a simple initial field geometry, a uniform B_z field; in subsequent sections we consider the evolution of B_z fields with zero net flux, uniform B_y fields, and mixtures of these cases.

In the two-fluid systems there are two identifiable limits in which the single-fluid results should apply: $\gamma = 0$ and $\gamma \rightarrow \infty$. When $\gamma = 0$ the ions are completely decoupled from the neutrals and their evolution will be as a single fluid with the ion density and ion Alfvén speed determining the final magnetic energy levels. In the other limit, the system will again behave as a single fluid, but with the *total* density determining the Alfvén speed and saturation energies. BB point out that the linear properties of the two-fluid system can be understood in terms of the “effective” density of the system, which varies between ρ_i and $\rho_i + \rho_n$ depending on the strength of the coupling. Since $\lambda_c \propto v_A = B/4\pi\rho^{1/2}$, the scaling relation (6) implies that the ratio of the magnetic energy in the decoupled ($\gamma = 0$) limit to the magnetic energy in the fully coupled ($\gamma = \infty$) limit will be $f^{1/2}$, for fixed initial magnetic field strength. We will explore the properties of the transition region between these two limits by varying the drag coefficient γ , the ionization fraction f , and other variables such as the equation of state and initial field strength in a number of different models.

3.2.1. A fiducial run

We begin our discussion with a baseline simulation against which to compare other models. This fiducial run (Z17) is a two-fluid shearing box with $31 \times 63 \times 31$ resolution, the standard survey resolution. (The complete list of vertical field simulations is provided in Table 1.) We set the neutral density $\rho_n = 1$, and the neutral sound speed $c_s = L_z\Omega$, with $L_z = 1$ and $\Omega = 10^{-3}$. The ion fraction is set to $f = 0.1$. This, together with a the drag coefficient $\gamma = 0.01$, yields a coupling frequency of $\gamma\rho_i/\Omega = 1.11$, just above the critical value. We use an isothermal equation of state, and assume a ratio of ion to neutral mass m_i/m_n of $30/2.33 = 12.9$. The ion sound speed is equal to $c_{si} = (m_i/m_n)^{1/2}$. The

assumption that the ions and neutrals have the same temperature establishes the relative pressures. The initial field is a uniform B_z field with strength $\beta_i = 80$, which corresponds to a value of $kv_{Ai}/\Omega = 0.28L_z/\lambda$. From the linear dispersion relation [eq. (24) of BB] we find that the unstable growth rates increase with increasing wavenumber, from a rate of 0.15Ω for $\lambda = L_z$ to 0.43Ω for $\lambda = L_z/4$. Smaller wavelengths are also unstable with comparable growth rates, up to the limit of $\lambda = 0.068L_z$, but such wavelengths are not well resolved.

The uniform initial conditions are perturbed with small, random fluctuations in the ion and neutral pressures. The magnetic field energy grows exponentially for the first three orbits before leveling out after orbit 4 (Fig. 2). The numerical growth rate of the instability is computed from the slope of the radial field energy density curve. The radial field perturbation grows at a rate of 0.27Ω , equal to the analytic value for $\lambda = L_z/2$. At 4.6 orbits plots of variables such as the B_x magnetic field show significant $\lambda = L_z/4$ structure. At this point, the system is largely axisymmetric, having the appearance of the channel solutions previously seen in pure B_z single fluid simulations (Hawley & Balbus 1992; HGB95).

At orbit 15 the toroidal field is dominated by a nearly axisymmetric $\lambda = L_z$ structure. The ions are greatly affected by the field since the toroidal field is now superthermal with $\beta_i = 0.6$. Filaments of high density ions are sandwiched between these regions of strong toroidal field (Fig. 3). The maximum ion density in the filaments is 2.5 times the average value. Since the neutral density has a much smaller relative variation, the ionization fraction in the filaments has gone up by a comparable amount. The neutral density plot shows much less small scale structure; the neutrals are dominated by trailing $m = 1$ pressure waves that are nearly independent of z . These have a maximum $\delta P_n/P_n$ of about 10%. Thus considerable separation of the ions from the neutrals occurs when the coupling frequency is comparable to the orbital frequency.

Figure 2 shows significant magnetic energy fluctuations after saturation. Representative values are obtained by time and space averages; some of these values are listed in Table 2. The time-averaged magnetic field energy after saturation is $B_y^2/8\pi = 0.011(L_z\Omega)^2$; the majority of the energy is in the toroidal field with $B_x^2/B_y^2 = 0.048$, and $B_z^2/B_y^2 = 0.035$. Since the toroidal field grows by both the action of the instability and the background shear flow, the amplitude of the poloidal fields provides the best measure of the turbulence. In this simulation the poloidal fields are considerably smaller than in single fluid runs. For example, in the fiducial run of HGB95 $B_x^2/B_y^2 = 0.32$, and $B_z^2/B_y^2 = 0.10$. Interestingly, the average magnetic field energy in the two-fluid system lies below both of the two single-fluid limits given by equation (6), either the one appropriate for the ions alone, or the one appropriate to the total density of ions plus neutrals. This implies that near the critical coupling frequency the neutrals primarily act as a drag to reduce the vigor of the field amplification, the MHD turbulence and the resulting transport.

The time-averaged perturbed kinetic energies in the ions are $\frac{1}{2}\langle\rho v_x^2\rangle_i = 6.8 \times 10^{-4}(L_z\Omega)^2$, $\frac{1}{2}\langle\rho\delta v_y^2\rangle_i = 3.0 \times 10^{-4}(L_z\Omega)^2$, $\frac{1}{2}\langle\rho v_z^2\rangle_i = 7.0 \times 10^{-5}(L_z\Omega)^2$. The evolution of the ion and neutral kinetic energy is depicted in Fig. 4. The volume-averaged kinetic energy of the neutrals evolves closely with that of the ions, except that it is larger by nearly the ratio ρ_n/ρ_i . The ion velocities are slightly larger on average.

As in the single-fluid case, angular momentum is transported outward by the Reynolds stress (both neutral and ion) and by the Maxwell stress. The Maxwell term is the largest stress component with $-\langle B_x B_y/4\pi\rangle = 0.0034(L_z\Omega)^2$; the neutral and ion Reynolds stresses

are 2.4×10^{-3} and $3.5 \times 10^{-4}(L_z\Omega)^2$ respectively. The ion Reynolds stress is proportionally larger than that of the neutrals, once the neutral to ion density ratio is factored out. In these units the sum of the stresses is equal to the Shakura-Sunyaev α value. Single fluid simulations find that while the ratio of total stress to the total pressure can vary substantially from one simulation to another, the ratio of the stress to the *magnetic* pressure is more nearly constant. The direct dependence of the stress on the magnetic pressure reflects both the fundamental role that the magnetic field plays in driving both the Maxwell and Reynolds stresses, as well as the high degree of correlation between the radial and toroidal field components. Clearly this remains true for ion-neutral systems. In the fiducial run $\alpha_{\text{mag}} = 0.61$, a value comparable to that seen in the single-fluid z -field simulations. Despite its lower relative value compared with the single-fluid simulation, the radial field remains highly correlated with the toroidal. The ratio $\langle B_x B_y \rangle / \sqrt{\langle B_x^2 \rangle \langle B_y^2 \rangle}$ is nearly 1 during the linear growth phase and has an average value of 0.7 after saturation.

The existence of unstable wavenumbers with large values, and the relatively low growth rate observed in the magnetic field, suggests that resolution may be influencing the simulation. Resolution can be especially important for ion-neutral simulations, because they typically have a wider range of rapidly growing wavelengths and physically important lengthscales compared to the single fluid system. For the parameters of the fiducial run, this is certainly true, and more grid zones should be required to resolve the linear growth phase adequately compared to the one-fluid system. Run LZ1 doubles the resolution of the fiducial run to $63 \times 127 \times 63$ grid zones while maintaining all other initial parameters. The observed growth rate for the magnetic field in the high resolution run is 0.35Ω (see Fig. 2), 30% larger than in the lower resolution run. The most obvious mode seen in density plots during the linear growth phase has $L_z/\lambda = 6$. Although ultimately both the low and high resolution simulations are dominated by the largest scales, resolution remains an important factor throughout the simulation. The high resolution simulation has 1.8 times as much magnetic energy as the fiducial run, when compared over the same time interval after saturation. The total stress is larger by a factor of 1.4.

3.2.2. Effect of ionization fraction

In the next set of simulations, we investigate the effect of the ionization factor by comparing the fiducial run to model Z20 with $f = 0.01$ and $\gamma = 0.1$, and model Z21 with $f = 0.001$ and $\gamma = 1$. We retain the same initial Alfvén speed $v_{Ai} = 0.044(L_z\Omega)$ as used in the fiducial run. Because we hold the Alfvén speed constant, the initial B_z magnetic field decreases as $f^{1/2}$. Table 2 lists time and space averaged values after saturation for this set of runs.

Although the parameter $kv_{Ai}/\Omega = 0.28L_z/\lambda$ is the same from one run to the next, the linear growth rates for the resolvable vertical wavelengths decrease with f (BB). For $\lambda = L_z$ the linear growth rates are 0.15, 0.047, and 0.015Ω ; for $\lambda = L_z/2$ the rates are 0.27, 0.093, and 0.03Ω . The measured growth rates for B_x in the simulations are 0.27, 0.072, and 0.016Ω for $f = 0.1, 0.01, \text{ and } 0.001$ respectively.

Despite the reduced growth rates, the total magnetic field *amplification* is comparable in all three runs, about two orders of magnitude in energy. The time-averaged magnetic

energy after saturation in these runs is 1.2×10^{-2} , 1.1×10^{-3} , and $2.0 \times 10^{-4}(L_z\Omega)^2$. These correspond to similar saturation amplitudes in the ion Alfvén speed, $v_{Ai}^2 \sim 0.1 (L_z\Omega)^2$ (Fig. 5). The majority of the magnetic energy is in the toroidal component. Since the saturated magnetic energy is proportional to f , the total stress is similarly proportional to f as is the Shakura-Sunyaev α parameter, defined with respect to the total pressure (neutral plus ion pressure). More significantly, the relative strength of the radial field compared to the toroidal declines with f . This means that the average α_{mag} also declines with f ; $\alpha_{\text{mag}} = 0.6$, 0.2 , and 0.1 in these three runs.

As in the fiducial run, the ions are squeezed into vertically thin sheets lying between regions of strong toroidal field; the lower the initial ionization fraction, the greater the compression. At a representative late time in runs Z17, Z20, and Z21, the maximum ion densities are 2.5, 2.6 and 4.2 times the initial value. The neutrals look similar in all three runs, again dominated by nearly z -independent trailing pressure waves.

Because the three models saturate at comparable ion Alfvén speeds, we conclude that the final state depends most strongly upon the ion density, that is, the effective inertia for the instability remains close to ρ_i . At coupling frequencies ~ 1 the role of the neutrals is mainly that of a sink for the turbulence. This is consistent with the observation that the magnetic energies in these simulations are smaller than predicted from equation (6) for a single-fluid with density equal to ρ_i .

While these results imply an increasingly small angular momentum transport for increasingly small ionization factors, this is partly because we have chosen to initialize this ensemble of simulations with constant Alfvén speed. An alternative is to begin with constant magnetic energy density. For example, a model with $f = 0.001$ is still unstable even with the field as strong as in the fiducial $f = 0.1$ simulation. With this strength of magnetic field and with $f = 0.001$, we have $\beta_i = 0.67$ initially, and $kv_{Ai}/\Omega = 8.85L_z/\lambda$. The analytic growth rate is 0.35 for the $\lambda = L_z$ mode. When such a run (Z23) is performed, however, the observed growth rate is only 0.15Ω compared with 0.27Ω in the fiducial run. The field is sufficiently strong (relative to the ion pressure), that compressibility is important, and this reduces the growth rate below the weak-field, incompressible value obtained from equation (24) of BB.

The saturated magnetic field energy in Z23 is lower than in the fiducial run, with $B^2/8\pi = 1.3 \times 10^{-3}(L_z\Omega)^2$. This is sufficiently strong that $\beta_i = 0.06$ on average. The dominance of the magnetic pressure is again reflected in the narrow, nearly axisymmetric sheets of ions surrounded by strong toroidal field. At the end of the run, the maximum ion density is 8 times the initial value, the largest relative compression of any of this series of runs. The ion sheets have a similarity of appearance to the channel solutions seen in the single fluid simulations, except that here field amplification stops and the growth of the nonaxisymmetric parasitic instability is suppressed or significantly reduced. Hence, the thin ion sheets endure. Despite a collisional frequency $\sim \Omega$, the ions and neutrals are not sufficient well coupled to overcome the complete dominance of the magnetic field on the ion evolution. The perturbed ion velocities are larger than those of the neutrals. The neutrals are again modified by the presence of nearly z -independent trailing pressure waves, except that the amplitude of these waves is now only $\delta P_n/P_n = 0.01$.

The time-averaged Maxwell stress in Z23 is $4.8 \times 10^{-4}(L_z\Omega)^2$, the ion Reynolds stress is $5.5 \times 10^{-7}(L_z\Omega)^2$, and the neutral Reynolds stress is $7.5 \times 10^{-5}(L_z\Omega)^2$. The stress is dominated by the Maxwell component which remains proportional to the magnetic energy,

with $\alpha_{\text{mag}} = 0.4$. The ion Reynolds stress is proportionally larger than the neutral stress by a factor of 7, but, due to the low ion fraction, its absolute value makes no significant contribution.

To summarize, we have examined three decades in ionization fraction with coupling frequencies near the orbital frequency. The observed numerical growth rates are consistent with the linear analysis of BB. Further, we find that these collision frequencies are insufficient to involve the neutrals in the evolution beyond providing a drag. The saturation amplitudes are determined by the ion Alfvén frequency, and low β_i values. Because saturation is determined mainly by the ions, and magnetic equipartition with the ion thermal energy, ion-neutral systems with very low ionization fractions and weak coupling would be expected to saturate at small magnetic field strengths.

3.2.3. *Effect of the collision frequency*

The analysis of BB highlights the importance of the ratio of the collision frequency to the epicyclic frequency. In the simulations described so far we have maintained the collision frequency near its critical value, i.e., comparable to the epicyclic frequency. We next investigate the effects of altering the collision frequency by modifying the drag coefficient γ . How does the turbulent magnetic energy vary as the coupling frequency is increased? At what point as the coupling frequency is increased do the neutrals couple strongly enough with the ions to be significantly affected by the MHD instability? At what value is the coupling frequency so low that the ions essentially decouple from the neutrals?

To investigate these questions, we run simulations with the same ionization fraction and initial magnetic field strength, but with different values of the drag coefficient γ . We begin with the initial conditions of the fiducial run, $f = 0.1$ and initial field strength $v_{Az_i} = 0.044L_z\Omega$, and set $\gamma = 0.001$ in run Z24, $\gamma = 0.1$ in Z25, and $\gamma = 1.0$ in Z28. Along with the fiducial run, this produces an ensemble of simulations with $\gamma\Omega/\rho_i = 0.111, 1.11, 11.1$ and 111.1 . Time and space averaged values from these simulations are given in Table 3.

The evolution of the magnetic energy in these simulations is shown in Figure 6. Along with the two-fluid runs, this figure includes two single-fluid simulations labeled C1 and C2. Run C1 has $\rho = 0.111$ (the same as ρ_i in the fiducial run) and C2 has $\rho = 1.111$ (the same as $\rho_i + \rho_n$ in the fiducial run). We use the fiducial run’s initial magnetic field strength for both these simulations, hence C1 and C2 have different initial values of the Alfvén speed, specifically $v_A/\Omega = 0.044$ and 0.139 . In both of these control simulations, turbulent saturation occurs after three orbits, with time-averaged magnetic energies of $0.025(L_z\Omega)^2$ and $0.083(L_z\Omega)^2$. While these values are somewhat below that predicted from the HGB95 empirical relationship (6), the ratio of the turbulent magnetic energies in these two runs is 0.30, consistent with the functional dependence expressed in equation (6).

The $\gamma = 0.001$ run (Z24) is similar to the low density single fluid calculation (C1). The ions are again squeezed into the very narrow filaments between strong magnetic fields while the neutrals are barely disturbed. This run is the first case discussed where the ion kinetic energy exceeds the neutral kinetic energy. The squeezing of the ions by the magnetic field

is sufficiently great that the ions sheets become effectively one zone wide and the simulation ends. An isothermal single-fluid simulation behaves like Z24. The C1 run uses an adiabatic equation of state; the additional pressure keeps the fluid sheets resolved, permitting the computation to continue. Again, this demonstrates that compressibility effects become important when $\beta < 1$.

The differences between the $\gamma = 0.01$ run (Z17) and the $\gamma = 0.1$ run (Z25) are small but significant. The magnetic field energies are comparable, but Z25 has a 25% larger average radial magnetic field strength, and greater neutral Reynolds stress leading to a 20% larger α value. Thus, an increase by 10 in the coupling frequency has had some influence on the saturation level, but has not yet brought the magnetic energies to near their single fluid values.

When the drag coefficient is increased to $\gamma = 1$ (Z28) the collisional frequency exceeds the orbital frequency by 111. The resulting turbulent magnetic energy is significantly larger than in the fiducial run, and continues to grow slowly during the simulation. The average values between orbits 10 and 14 are $B_x^2/8\pi = 0.0049(L_z\Omega)^2$, $B_y^2/8\pi = 0.050(L_z\Omega)^2$, and $B_z^2/8\pi = 0.0017(L_z\Omega)^2$, about 70% of the values seen in the single fluid simulation C2.

Table 2 lists the ratios of the ion to neutral kinetic energies. If the two fluids were fully coupled, this ratio, and a similar ratio for the Reynolds stress, would be precisely the ionization fraction. This provides one measure of the effective coupling in the turbulent state. As the coupling frequency increases, the ratio of the Maxwell stress to neutral Reynolds stress increases toward the single-fluid range of 4–5. The ion Reynolds stress also increases, but even for run Z28 it is not yet quite one tenth the neutral value. It appears that coupling frequencies must be $\gamma\Omega/\rho_i \gtrsim 100$ before the evolution becomes similar to that of the fully ionized fluid.

As another test of the role of γ , we compare a series of $f = 0.01$ runs with γ values equal to 0.01, $\gamma\Omega/\rho_i = 0.1$ (Z19), $\gamma = 0.1$, $\gamma\Omega/\rho_i = 1$ (Z20), and $\gamma = 10$, $\gamma\Omega/\rho_i = 100$ (Z27). In the least well-coupled model (Z19) the ions are squeezed into very narrow filaments between regions of strong toroidal field. With increasing γ the ions are less confined into coherent sheets, more turbulent, and more like the single-fluid simulations. The angular momentum transport is again dominated by the Maxwell stress. In the three runs, $\alpha_{\text{mag}} = 0.2, 0.3,$ and 0.4 . The increase in α_{mag} reflects the larger values of radial field that are obtained with increasing γ . In Z27, the ratio of the ion to neutral kinetic energy and ion to neutral Reynolds stress are nearly equal to the ionization fraction, indicating good coupling. In order of increasing γ , the turbulent magnetic energies are 2.6×10^{-3} , 1.0×10^{-3} , and $6.7 \times 10^{-3}(L_z\Omega)^2$. These energies are dominated by the toroidal field; the ratios of toroidal to radial magnetic energy are 0.006, 0.009, and 0.027. Although the best-coupled run (Z27) has the largest magnetic energy, its value is still a factor of 3 below the single-fluid prediction with density ρ_{tot} . It should be noted that in terms of the total gas pressure, the initial field is quite weak with $\beta_{\text{tot}} = 10^5$. For a single fluid simulation with this strength field, the critical wavelength is less than the grid spacing, so this simulation is somewhat under-resolved.

Next, we consider a well-coupled model (Z22) with a stronger initial field and a lower ionization fraction, specifically, $f = 0.001$ and $\gamma = 100$. This raises the collision frequency to $\gamma\rho_i/\Omega = 100$. The initial field is set to $\beta_i = 0.1$. The instability develops rapidly as a channel solution (two channels in the vertical direction), then saturates at 4.5 orbits as the channels break up into turbulence. Despite beginning with a strong field relative to the ions, the coupling is sufficient to raise the effective inertia of the system, and to ensure

that the neutrals become fully turbulent as well. The magnetic energy at the end of the simulation is $0.036(L_z\Omega)^2$ which corresponds to $\beta = 28$, and $\beta_i = 0.002$. As always, the Maxwell stress is the largest with a value of $0.018(L_z\Omega)^2$, but the neutral Reynolds stress is now also significant at $0.0073(L_z\Omega)^2$. The ion Reynolds stress is smaller by a factor of f . The value of α is 0.025, while $\alpha_{\text{mag}} = 0.7$. Overall the evolution is much like that for a single fluid. If the collision frequency is sufficiently large, full MHD turbulence and significant angular momentum transport are recovered, even for low ionization fractions.

To explore the other extreme, and to follow the approach to decoupling in the low- γ limit, we run 4 models with $f = 0.01$ and $\gamma = 0.1, 0.05, 0.01$, and 0.001 (Z4a, Z5a, Z6a, Z7a). These models use an adiabatic equation of state with an initial ratio of ion to neutral gas pressure of 4×10^{-4} . The adiabatic equation of state prevents the magnetic field from squeezing the ions into numerically unresolvable sheets. The runs of this group are all very similar except for Z7a. Although all four runs end up with similar toroidal field energies, only Z7a has a substantial radial field energy; this results in a larger total Maxwell stress. The average energy in the radial ion velocity fluctuations is almost two orders of magnitude larger in Z7a compared with the others. The observed growth rate in Z7a is comparable to the single fluid case. These results indicate that when $\gamma\rho_i/\Omega \lesssim 0.01$ the ions and neutrals behave essentially as two distinct fluids.

3.2.4. Other effects

BB determined that in two-fluid systems the presence of a strong toroidal field can affect growth rates. We demonstrate this point by rerunning the fiducial run with the addition of a strong toroidal field with $B_y = 10B_z$ (YZ1). Such a field has $v_{A\phi} > 1.6c_{si}^2$, and with $\gamma\rho_i/\Omega = 1.11$ the growth rates should be significantly affected (BB). Indeed, we find that the growth rate of the perturbed magnetic field drops to 0.18Ω . After saturation at orbit 7 the radial magnetic and kinetic energies are reduced compared to the fiducial run, and this reduces the total transport to $\alpha = 0.002$. The total magnetic energy is slightly larger than in the fiducial run, although this is mainly because here the toroidal field *began* at this level.

The results discussed so far point to a significant role for compressibility in the growth and saturation of the instability. The ions are strongly affected by magnetic pressure when $\beta_i < 1$ and the ion-neutral coupling frequency is near or below $\sim \Omega$. To further study the role of compressibility, we rerun the fiducial case with the ion and neutral masses equal (run Z18); this increases the ion pressure. Both this run and the fiducial run are the same during the linear growth phase. Run Z18, however, saturates at a magnetic field energy level that is about twice that of Z17. Since the saturated β_i value is larger in Z18 (even though the magnetic field is stronger than in Z17), the ions are less tightly confined. This is consistent with the conclusion that if the saturated magnetic energies yield $\beta > 1$, the gas pressure remains mostly unimportant, whereas if $\beta < 1$, pressure can bring field amplification to an end. The effects of pressure are particularly noticeable in the two-fluid simulations because, in contrast to previously studied single-fluid models, the magnetic pressures in the saturated states generally have $\beta_i < 1$. (This depends, of course, on how we chose to initialize the simulations. Here, the initial ion pressure is generally much less than the

neutral pressure, and the neutral pressure is chosen so that $c_{sn} = L_z \Omega$.) If the coupling is sufficiently weak such that the effective inertia for the magnetic instability is close to that provided by the ions alone, the pressure prevents the magnetic field from becoming much stronger than equipartition with the ion pressure.

3.3. Zero net B_z fields

The structure associated with the nonlinear regime of the instability in the weakly-coupled pure B_z field simulations described above is dominated by the persistence of the channel solution in the form of narrow, nearly axisymmetric sheets of ions. This is in contrast to the single-fluid simulations, where parasitic instabilities inevitably cause the channel solution to break up into MHD turbulence (HGB95). The axisymmetric coherence of the channel solution is lost when the initial B_z field is not uniform. To study this in the two-fluid case, we have performed simulations which begin with fields of the form $B_z \propto \sin(x)$ so that there is zero net flux through the computational domain.

Our first zero net B_z field simulation (ZN1) is computed using nearly the same parameter values as the fiducial pure B_z field simulation, i.e., $\beta_i = 80$, $f = 0.1$, and $\gamma = 0.009$, yielding a coupling frequency of $\gamma \rho_i / \Omega = 1$. We adopt an isothermal equation of state, and use the standard resolution to evolve the model. Once again, we observe exponential growth of the magnetic energy, with saturation at an amplitude of $0.01(L_z \Omega)^2$ occurring near 5 orbits. In the saturated state, the Maxwell stress dominates the Reynolds stress, with $-\langle B_x B_y / 4\pi \rangle = 0.002(L_z \Omega)^2$ averaged over the first 10 orbits. These values are all consistent with those reported for the fiducial run Z17. As is the case in single-fluid zero net B_z field simulations (Hawley, Gammie, & Balbus 1996), the amplitude of the turbulence decreases significantly after saturation, but it never dies completely away; the magnetic energy remains at least a factor of 5 larger than in the initial state.

We have also computed the evolution of a zero net B_z field with a smaller drag coefficient, i.e. $\gamma = 0.002$ yielding $\gamma \rho_i / \Omega = 2/9$, but all other parameters identical to ZN1. This model (ZN2) evolves in a similar fashion, but with a smaller initial growth rate that produces saturation at a slightly later time (6 orbits). The amplitude of the saturated magnetic energy, kinetic energy, Maxwell and Reynolds stress are all similar to the pure B_z field simulation Z24. However, unlike Z24, the ions do not have a channel-like structure.

The turbulence observed in these simulations is driven by the instability acting upon the ions. Because of drag, turbulent motions are also driven in the neutrals. However, the ions and neutrals will be coupled only on scales greater than $L_{drag} = v_{An} / \gamma \rho_i$. Since in these models the magnetic field saturates at $v_{Ai} \sim c_{si}$ we can write

$$L_{drag} = \left(\frac{f}{1-f} \right)^{\frac{1}{2}} \left(\frac{m_n}{m_i} \right)^{\frac{1}{2}} \frac{L_z \Omega}{\gamma \rho_i} = 0.09 \frac{L_z \Omega}{\gamma \rho_i}. \quad (7)$$

For the parameter values adopted for run ZN1, $L_{drag} = 0.09$, and for ZN2 $L_{drag} = 0.42$. To investigate whether there is any quantifiable difference between the turbulence in the ions and neutrals on scales above and below L_{drag} , we plot in Figure 7 the power spectrum

of the specific kinetic energy in the fluctuations of the z -component of velocity (δv_z^2) in both the ions and neutrals for ZN1 (top panel) and ZN2 (bottom panel). In run ZN1, the energy in velocity fluctuations in the ions and neutrals is virtually identical on all scales. Given the wavenumber associated with the drag length is $k_{drag} = 22\pi/L_z$, which is more than the largest wavenumber representable at the standard resolution, this result is to be expected. However, the power spectrum for run ZN2 shows a systematic difference between the ions and neutrals above a wavenumber of about 10; the energy associated with velocity fluctuations in the neutrals is less than that of the ions by about an order of magnitude. In this case, $k_{drag} = 4.8\pi/L_z$, which is in agreement with the observed location of the break in the power spectrum. In summary, we find that on scales less than L_{drag} the ions and neutrals are poorly coupled, and the structure of the neutrals is very smooth, whereas on scales larger than L_{drag} the ions and neutrals are well coupled and exhibit a decreasing power law spectrum with identical amplitude.

3.4. Uniform B_y fields

The analysis of BB considered axisymmetric, vertical wavenumber modes. A remaining question is whether purely toroidal fields are also unstable in the two-fluid system. Toroidal fields exhibit a nonaxisymmetric instability in the single-fluid system, as found both analytically and numerically (Balbus & Hawley 1992; HGB95; Matsumoto & Tajima 1995). In the fully ionized disk, the observed growth rates are lower than with vertical fields, but not dramatically so. The turbulent magnetic energy densities that result are lower than those seen in the vertical field simulations by about an order of magnitude, although they are still proportional to the geometric average of the background field strength and the field strength corresponding to the largest possible unstable wavelengths given the dimensions of the simulation box, L_y (HGB95). Outward angular momentum transport is produced with a total stress that remains proportional to the magnetic pressure, with $\alpha_{mag} \sim 0.5$.

The nonaxisymmetric instability must be present for the two-fluid system as well, at least in completely coupled and decoupled limits. Here we investigate what happens near the critical value of the collision frequency, $\gamma\rho_i/\Omega = 1$ with the series of toroidal field runs listed in Table 4. Figure 8 shows the time evolution of the toroidal and radial magnetic field energies for the models listed in Table 4. Table 5 lists the value of some averaged quantities after saturation for these runs.

The first simulation (Y5) has an ion fraction of $f = 0.1$ and a drag coefficient $\gamma = 0.01$. Again we use an isothermal equation of state, and assume a ratio of ion to neutral mass m_i/m_n of 30/2.33. The initial field is a uniform B_y field with strength $\beta_i = 10$, which corresponds to a value of $kv_{Ai}/\Omega = 0.125L_y/\lambda$. The perturbations grow slowly in this simulation, leveling out after 20 orbits, continuing to grow very slowly after that time. Relatively little total field amplification occurs, with the average magnetic field strength near the end of the run (46 orbits) equal to 2.1×10^{-3} . Total stress is also small, with $\alpha = 4.4 \times 10^{-4}$ and $\alpha_{mag} = 0.22$. The ions are found in small scale features that have a mostly $m = 1$ structure. The perturbation in the neutrals consists of trailing $m = 1$ waves that are nearly independent of height z .

In these simulations, the fastest growing unstable wavelengths are short compared to the computational domain size, although the full range of unstable wavelengths is large and includes lengths comparable to L_y . Because of this, numerical resolution will play an important role in the linear growth and possibly in the final saturation of the instability. To measure this effect, we repeat the fiducial toroidal field run with twice the resolution, i.e., $63 \times 127 \times 63$ (LY1). The observed growth rate during the initial orbits is increased. At the end of the high resolution run the magnetic energy is twice the value at the same time in Y5. At this point the growth rate levels off to a value much like the lower resolution simulation. Given the low growth rates it seems impractical to carry out this simulation to late times, but it is clear that resolution significantly affects the initial evolution of these toroidal field models. In analyzing these runs, therefore, we will focus on qualitative effects and relative values of quantities.

In the next model (Y6) we increase the initial B_y field to $\beta_i = 0.8$, which corresponds to $kv_{Ai}/\Omega = 0.441L_y/\lambda$. This is the same ion Alfvén speed as in the toroidal plus B_z run discussed above (YZ1). The initial growth rate is larger than in Y5, but at saturation, which occurs at orbit 15, the radial field energy has risen only to $1.5 \times 10^{-4}(L_z\Omega)^2$. Again the stress levels are low, with $\alpha = 8.4 \times 10^{-4}$ and $\alpha_{\text{mag}} = 0.072$. The low stress levels, and, in particular, the low level of α_{mag} is due to the weak amplification of the poloidal field, and its small value compared to the initial toroidal field.

Generally, larger growth rates are obtained when $kv_A/\Omega \sim 1$, but with Y6 we are already in the regime where the initial field is superthermal (in the ions). The linear analysis of BB and the single fluid analysis of Balbus & Hawley (1992) found that compressibility becomes important for such strong fields, reducing the effective growth rate. In the present simulations the ion pressure can be increased and the value of β_i decreased for a given field strength if the ion and neutral masses are set equal, $m_i = m_n$. We repeat the above two runs with this change, carrying out runs with $v_{Azi}/\Omega = 0.441$ (Y7; compare with Y6) and $v_{Azi}/\Omega = 0.125$ (Y8; compare with Y5). The increase in ion pressure has relatively little effect on the evolution during the linear phase. After 20 orbits, however, the field in run Y8 grows to higher levels, suggesting that the ion pressure plays a significant role in the nonlinear evolution. This is consistent with the vertical field results discussed above. In contrast, comparing runs Y6 and Y7 (with $\beta_i = 0.8$ and 10.3 respectively) produces a noticeable difference during the linear phase. The growth rate is increased and the total field is amplified by a factor of 2.3 to $\beta_i = 4.4$. Angular momentum transport is similarly enhanced, with $\alpha = 0.008$ and $\alpha_{\text{mag}} = 0.33$. These runs confirm that compressibility can affect both the linear and nonlinear evolution of the instability whenever $\beta_i < 1$.

As the collision frequency increases, the system should approach that of a single fluid. To test this we repeat the fiducial run with the collision parameter increased to $\gamma\rho_i/\Omega = 111$ (Y9). In this run the initial growth through 15 orbits is quite similar to the first run (Y5), but poloidal field growth continues for a longer time than in Y5. At 40 orbits the field energies are still rising, and have twice the magnetic energy as Y5. The tight coupling means that the perturbed velocities in the two fluids have the same values on average.

4. Discussion

We have carried out a series of simulations to examine the behavior of the magnetorotational instability in partially-coupled ion-neutral systems. We find that weak vertical fields are unstable with growth rates consistent with the linear analysis of BB. The initial evolution of the vertical field instability behaves much like the channel solution found in the single fluid simulations. This is consistent with the finding of BB that the unstable two-fluid mode with vertical magnetic field is still an exact local nonlinear solution to the equations of motion. In our simulations, if the ion fraction and the collision frequency are low the channel solution can persist, squeezing the ions into narrow channels between regions of strong toroidal field. As β_i decreases, the simulation ends when the channels become one grid zone thick.

Brandenburg & Zweibel (1995) have emphasized that because ion-neutral coupling acts as a nonlinear diffusion process, certain initial field configurations can evolve into thin current sheets. Because we are far from the well-coupled limit studied by Brandenburg & Zweibel, it is difficult to assess the relative importance of nonlinear diffusion due to ambipolar diffusion in these simulations. We have identified the primary mechanism for the growth of the narrow sheets in the vertical field simulations with the “channel solution” of the magnetorotational instability. Precisely the same thin sheets are observed in single-fluid (fully ionized) simulations, and in the ions in the nearly-decoupled limit. In both cases, the fluid is squeezed by an exponentially growing field until the channel becomes one zone thick and the simulation ends. Further, the zero-net-field two-fluid simulations presented here, which do not produce a channel solution, also avoid the formation of large-scale current sheets. It remains an open question whether the nonlinear diffusion of Brandenburg & Zweibel (1995) increases the tendency to thin sheets, or otherwise affects the turbulent state in ion-neutral systems.

Through a series of simulations with varying drag coefficient γ we have explored the transition from the fully coupled to the completely uncoupled limit. We find that there are important two-fluid effects over the range $0.01 < \gamma\rho_i/\Omega < 100$. In simulations at the upper end of this range the ions and neutrals are strongly coupled, although the turbulence levels remain somewhat below the single-fluid case. Our results are consistent with the simulations of Mac Low et al. (1995) who found significant ambipolar diffusion when $\gamma\rho_i/\Omega = 30$, but little apparent diffusion at a value of 300.

At the other extreme, the weakly coupled limit with $\gamma\rho_i/\Omega \sim 0.01$, the perturbed ion kinetic energy actually exceeds that of the neutrals (despite an ionization fraction of 0.01), and the magnetic energy is increased over levels found in the results for larger drag coefficient values. This signals the almost complete separation of the ion and neutral fluid.

When the collisional frequency is comparable to the orbital frequency, $\gamma\rho_i/\Omega \sim 1$, the nonlinear evolution of the instability is primarily controlled by the ion density. Magnetic field saturation occurs near or just above equipartition with the ion pressure. Hence the saturated magnetic field energy goes down with ionization fraction, which, in turn, means that the total angular momentum transport is also proportional to f .

The instability transports angular momentum in the two-fluid system, through a combination of Maxwell and Reynolds stresses. The total stress is proportional to the magnetic energy density in all simulations. The constant of proportionality (α_{mag}) depends on the amount of radial field amplification relative to the toroidal field. With good coupling or larger ionization fractions α_{mag} is comparable with the single-fluid value (HGB95). Weak coupling (but not completely uncoupled) and low ionization fractions produce reduced values.

Because the neutrals are coupled to the magnetic field only through drag with the ions, the effect of the instability on the neutrals depends on the size of the drag coefficient. The neutral system alone is hydrodynamic, and as such is stable to hydrodynamic perturbations (BHS96). The ion velocity fluctuations are correlated so as to produce a net positive ion Reynolds stress, and that correlation is conveyed to the neutrals. However, because the neutrals lack direct coupling to the magnetic fields, a positive Reynolds stress acts as a sink in the neutral angular velocity fluctuation equation. In the intermediate coupling regime this apparently works to damp the strength of the ion turbulence to levels below what would be seen with the ion system fully decoupled.

Why does gas pressure matter in these simulations and not in the single-fluid studies done previously? In the single-fluid simulations (HGB95) the gas pressure was largely irrelevant, in part because the box size was chosen so that $P = (L_z \Omega)^2$ and the largest unstable wavelength corresponded to a subthermal field. In the ion-neutral system as we have set it up here, fields that are superthermal in the ion pressure (i.e., have $\beta_i < 1$) can still be unstable. For small ionization fractions these fields will be very subthermal in terms of the total (neutral plus ion) pressure ($\beta \gg 1$). When $\gamma \Omega / \rho_i \sim 1$, the ion pressure significantly affects the nonlinear stage of the evolution, for both toroidal and vertical initial field models. The tendency for the ions to form thin sheets between regions of strong toroidal field is symptomatic. In some cases this reduces the vigor of the resulting turbulence. Stronger turbulence and more angular momentum transport can be obtained by decreasing the ion mass, and hence increasing the ion pressure (under the assumption of equipartition of thermal energy between the ion and neutral particles, $m_i c_{si}^2 = m_n c_{ni}^2$). We consistently find stronger turbulence with higher ion pressures.

When toroidal fields are included in the initial conditions along with vertical field, they can reduce linear growth rates, in accordance with the analysis of BB. However, the reduced growth rates have less of an effect once the nonlinear regime is reached. In fact, far from preventing the the growth of the instability, we find that purely toroidal initial fields are also unstable. However, the instability is significantly reduced for weak coupling if the toroidal field is superthermal. Although this is true in the single fluid case as well, there it was hardly an issue because $v_A \sim c_s$ was already a very strong field. Here, however, if $m_i > m_n$, the ion pressure can be substantially smaller than the neutral. If the ion fraction is small, the ion Alfvén speed can easily become large compared to the ion sound speed, despite a relatively weak toroidal field.

Numerical resolution is more important in these simulations than for the single fluid models. The presence of both ion and neutral components introduces additional lengthscales that can be quite disparate, as in the case of low ionization fractions and intermediate strength coupling. A Fourier analysis of the velocity fluctuations associated with the ions and neutrals shows that, as expected, on scales greater than $L_{drag} = v_{An} / \gamma \rho_i$, the ions and neutrals are well coupled with identical power spectra for velocity fluctuation, whereas on scales less than L_{drag} the fluctuations in the neutrals are at a considerably lower amplitude than those in the ions. Thus, L_{drag} represents an important lengthscale introduced into two fluid models that must be resolved numerically.

In summary, we expect that the two-fluid effects studied here will be appropriate to a transition region in protostellar or protoplanetary accretion disks between the inner, hot, and fully ionized regions, and the outer, cold, and essentially neutral regions. Our simulations suggest a more stringent criterion for good coupling than that obtained from the linear result of BB. We find that, while the linear instability is present for coupling

frequencies $\sim \Omega$, significant turbulence and angular momentum transport can only occur when coupling frequencies $\gamma\Omega/\rho_i > 100$. For weaker coupling, the magnetic energies are determined primarily by the ion density.

There are many interesting issues regarding this transition region in a protostellar disk that go beyond the limitations of this initial study. Here we have assumed that both the recombination and ionization timescales are much longer than the orbital period. In real systems, the ion density in structures such as the ion filaments may be limited by recombination. On the other hand, at the interface between weak and strong coupling, increasing the ionization fraction increases the efficiency of magnetic coupling, which in turn increases the level of turbulent heating thus raising the ionizational level yet higher. Investigating stability issues such as these, as well as the global structure and dynamics of weakly coupled disks, are fruitful areas for future research.

We thank Steven Balbus for valuable discussions, and Omer Blaes and Mordecai-Mark Mac Low for comments on the manuscript. This work is supported in part by NASA grants NAG-53058, NAGW-4431, and NSF grant AST-9423187 to J.H., by NASA grant NAG-54278 and NSF grant AST-9528299 to J.S., and by a metacenter grant MCA95C003 from the Pittsburgh Supercomputing Center and NCSA.

TABLE 1: Z FIELD SIMULATIONS

Model	f	γ	$\gamma\rho_i/\Omega$	m_i/m_n	$v_{Azi}/L_z\Omega$	Grid	Orbits	Comment
Z17	0.1	0.01	1.1	12.9	0.044	$31 \times 63 \times 31$	26	Fiducial
LZ1	0.1	0.01	1.1	12.9	0.044	$63 \times 127 \times 63$	13	High-Res
Z20	0.01	0.1	1.0	12.9	0.044	$31 \times 63 \times 31$	30	
Z21	0.001	1	1.0	12.9	0.044	$31 \times 63 \times 31$	71	
Z23	0.001	1	1.0	12.9	0.46	$31 \times 63 \times 31$	10	
Z24	0.1	0.001	0.11	12.9	0.044	$31 \times 63 \times 31$	4	
Z25	0.1	0.1	11.1	12.9	0.044	$31 \times 63 \times 31$	11	
Z28	0.1	1	111	12.9	0.044	$31 \times 63 \times 31$	14	
Z19	0.01	0.1	0.1	12.9	0.044	$31 \times 63 \times 31$	27	
Z27	0.01	10.	101	12.9	0.044	$31 \times 63 \times 31$	29	
Z22	0.001	100	100	12.9	1.25	$31 \times 63 \times 31$	63	
Z4a	0.01	0.1	1.0	2.1	0.044	$31 \times 63 \times 31$	32	Adiabatic
Z5a	0.01	0.05	0.5	2.1	0.044	$31 \times 63 \times 31$	32	Adiabatic
Z6a	0.01	0.01	0.1	2.1	0.044	$31 \times 63 \times 31$	24	Adiabatic
Z7a	0.01	0.001	0.01	2.1	0.044	$31 \times 63 \times 31$	19	Adiabatic
YZ1	0.1	1	1.1	12.9	0.044	$31 \times 63 \times 31$	14	
Z18	0.1	0.01	1.1	1	0.044	$31 \times 63 \times 31$	15	

**TABLE 2: TIME- AND VOLUME-AVERAGE VALUES
EFFECT OF IONIZATION FRACTION**

$\langle\langle\text{Quantity}\rangle\rangle$	Z17	Z20	Z21	Z23
f	0.1	0.01	0.001	0.001
$B_x^2/8\pi(L_z\Omega)^2$	5.3×10^{-4}	7.8×10^{-6}	1.8×10^{-7}	5.7×10^{-5}
$B_y^2/8\pi(L_z\Omega)^2$	1.1×10^{-2}	1.1×10^{-3}	2.0×10^{-4}	1.1×10^{-3}
$B_z^2/8\pi(L_z\Omega)^2$	3.8×10^{-4}	1.4×10^{-5}	1.2×10^{-6}	1.2×10^{-4}
$(\rho v_x^2)_i/2(L_z\Omega)^2$	6.8×10^{-4}	4.7×10^{-6}	7.0×10^{-7}	8.1×10^{-7}
$(\rho\delta v_y^2)_i/2(L_z\Omega)^2$	3.0×10^{-4}	5.5×10^{-7}	7.7×10^{-8}	1.4×10^{-7}
$(\rho v_z^2)_i/2(L_z\Omega)^2$	7.0×10^{-5}	3.2×10^{-7}	8.1×10^{-8}	1.3×10^{-7}
$(\rho v_x^2)_i/(\rho v_x^2)_n$	0.10	0.010	0.0010	0.0031
$(\rho\delta v_y^2)_i/(\rho\delta v_y^2)_n$	0.16	0.013	0.0010	0.0048
$(\rho v_z^2)_i/(\rho v_z^2)_n$	0.13	0.013	0.0017	0.0026
E_M/KE_i	11.8	200	5100	1200
$-B_x B_y/4\pi(L_z\Omega)^2$	3.4×10^{-3}	1.4×10^{-4}	9.0×10^{-6}	4.8×10^{-4}
$(\rho v_x v_y)_i/(L_z\Omega)^2$	3.5×10^{-4}	1.4×10^{-6}	1.8×10^{-8}	5.5×10^{-7}
$(\rho v_x v_y)_n/(L_z\Omega)^2$	2.4×10^{-3}	1.2×10^{-4}	1.7×10^{-5}	7.5×10^{-5}
Max/Reynolds _i ^a	9.7	100	510	870
Max/Reynolds _n	1.4	1.3	0.53	6.4
α	6.1×10^{-3}	2.6×10^{-4}	2.6×10^{-5}	5.6×10^{-4}
α_{mag}	0.61	0.23	0.13	0.42

^aMax/Reynolds_i is the ratio of the Maxwell stress to ion Reynolds stress. Similarly

Max/Reynolds_n is the ratio of the Maxwell stress to neutral Reynolds stress.

**TABLE 3: TIME- AND VOLUME-AVERAGE VALUES
EFFECT OF COUPLING CONSTANT**

$\langle\langle$ Quantity $\rangle\rangle$	Z24	Z17	Z25	Z28
γ	0.001	0.01	0.1	1.0
$B_x^2/8\pi(L_z\Omega)^2$	2.4×10^{-3}	5.3×10^{-4}	8.1×10^{-4}	4.9×10^{-3}
$B_y^2/8\pi(L_z\Omega)^2$	1.9×10^{-2}	1.1×10^{-2}	1.1×10^{-2}	5.0×10^{-2}
$B_z^2/8\pi(L_z\Omega)^2$	3.7×10^{-4}	3.8×10^{-4}	3.7×10^{-4}	1.7×10^{-3}
$(\rho v_x^2)_i/2(L_z\Omega)^2$	1.2×10^{-3}	6.8×10^{-4}	5.1×10^{-4}	1.3×10^{-3}
$(\rho \delta v_y^2)_i/2(L_z\Omega)^2$	1.7×10^{-3}	3.0×10^{-4}	1.4×10^{-4}	5.8×10^{-4}
$(\rho v_z^2)_i/2(L_z\Omega)^2$	2.3×10^{-4}	7.0×10^{-5}	8.7×10^{-5}	4.1×10^{-4}
$(\rho v_x^2)_i/(\rho v_x^2)_n$	1.04	0.10	0.11	0.11
$(\rho \delta v_y^2)_i/(\rho \delta v_y^2)_n$	5.4	0.16	0.13	0.12
$(\rho v_z^2)_i/(\rho v_z^2)_n$	0.65	0.13	0.12	0.11
E_M/KE_i	6.1	11.8	18	26
$-B_x B_y/4\pi(L_z\Omega)^2$	1.2×10^{-2}	3.4×10^{-3}	4.7×10^{-3}	2.4×10^{-2}
$(\rho v_x v_y)_i/(L_z\Omega)^2$	2.2×10^{-3}	3.5×10^{-4}	2.3×10^{-4}	6.4×10^{-4}
$(\rho v_x v_y)_n/(L_z\Omega)^2$	7.6×10^{-5}	2.4×10^{-3}	1.8×10^{-3}	5.5×10^{-3}
Max/Reynolds _i	5.2	9.7	20	37
Max/Reynolds _n	150	1.4	2.6	4.3
α	1.4×10^{-2}	6.1×10^{-3}	6.6×10^{-3}	3.0×10^{-2}
α_{mag}	0.63	0.61	0.54	0.53

TABLE 4: Y FIELD SIMULATIONS

Model	f	γ	$\gamma\rho_i/\Omega$	m_i/m_n	$v_{Azi}/L_z\Omega$	Grid	Orbits
Y5	0.1	0.01	1.1	12.9	0.125	$31 \times 63 \times 31$	46
LY1	0.1	0.01	1.1	12.9	0.125	$63 \times 127 \times 63$	19
Y6	0.1	0.01	1.1	12.9	0.441	$31 \times 63 \times 31$	32
Y7	0.1	0.01	1.1	1	0.441	$31 \times 63 \times 31$	17
Y8	0.1	0.01	1.1	1	0.125	$31 \times 63 \times 31$	50
Y9	0.1	1	111	12.9	0.125	$31 \times 63 \times 31$	42

**TABLE 5: TIME- AND VOLUME-AVERAGE VALUES
Y FIELD SIMULATIONS**

$\langle\langle$ Quantity $\rangle\rangle$	Y5	Y6	Y7	Y8	Y9
$B_x^2/8\pi(L_z\Omega)^2$	1.3×10^{-5}	1.5×10^{-4}	1.1×10^{-3}	7.1×10^{-5}	2.1×10^{-4}
$B_y^2/8\pi(L_z\Omega)^2$	2.1×10^{-3}	1.2×10^{-2}	2.4×10^{-2}	4.2×10^{-3}	5.6×10^{-3}
$B_z^2/8\pi(L_z\Omega)^2$	2.6×10^{-6}	8.9×10^{-5}	4.0×10^{-4}	1.7×10^{-5}	6.8×10^{-5}
$(\rho v_x^2)_i/2(L_z\Omega)^2$	5.9×10^{-5}	5.9×10^{-5}	5.6×10^{-4}	1.7×10^{-4}	1.5×10^{-4}
$(\rho \delta v_y^2)_i/2(L_z\Omega)^2$	1.6×10^{-6}	3.8×10^{-5}	3.3×10^{-4}	3.7×10^{-5}	4.1×10^{-5}
$(\rho v_z^2)_i/2(L_z\Omega)^2$	1.7×10^{-6}	1.7×10^{-5}	1.1×10^{-4}	1.2×10^{-5}	3.1×10^{-5}
$(\rho v_x^2)_i/(\rho v_x^2)_n$	0.094	0.097	0.10	0.11	0.11
$(\rho \delta v_y^2)_i/(\rho \delta v_y^2)_n$	0.11	0.19	0.21	0.15	0.11
$(\rho v_z^2)_i/(\rho v_z^2)_n$	0.12	0.10	0.096	0.11	0.11
E_M/KE_i	35	113.	27.	25	27.
$-B_x B_y/4\pi(L_z\Omega)^2$	1.8×10^{-4}	5.6×10^{-4}	5.7×10^{-3}	7.6×10^{-4}	1.4×10^{-3}
$(\rho v_x v_y)_i/(L_z\Omega)^2$	2.4×10^{-5}	3.4×10^{-5}	3.3×10^{-4}	5.8×10^{-5}	5.5×10^{-4}
$(\rho v_x v_y)_n/(L_z\Omega)^2$	2.4×10^{-4}	2.5×10^{-4}	2.4×10^{-3}	4.5×10^{-4}	5.0×10^{-4}
Max/Reynolds _i	7.6	17.	17.	13.	26.
Max/Reynolds _n	0.75	2.3	2.3	1.7	2.9
α	4.4×10^{-4}	8.4×10^{-4}	7.6×10^{-3}	1.1×10^{-3}	2.0×10^{-3}
α_{mag}	0.22	0.07	0.33	0.30	0.34

References

- Balbus, S. A., & Hawley, J. F. 1991, *ApJ*, 376, 214
Balbus, S. A., & Hawley, J. F. 1992, *ApJ*, 400, 610
Balbus, S.A., Hawley, J.F., & Stone, J.M. 1996, *ApJ*, 467, 76 (BHS96)
Blaes, O. M., & Balbus, S. A. 1994, *ApJ*, 421, 163 (BB)
Brandenburg, A., Nordlund, Å, Stein, R. F., Torkelsson, U. 1995, *ApJ*, 446, 741
Brandenburg, A., & Zweibel, E. G. 1995, *ApJ*, 448, 734
Cabot, W. 1996, *ApJ*, 465, 874
Cuzzi, J. N., Dobrovolskis, A. R., & Hogan, R. C. 1996, in *Chondrules and the Protoplanetary Disk*, ed. R. H. Hewins, R. H. Jones, & E. R. D. Scott (Cambridge: Cambridge Univ. Press), 35
Draine, B. T., Roberge, W. G., & Dalgarno, A. 1983, *ApJ*, 264, 485
Goodman J. & Xu, G. 1994, *ApJ*, 432, 213
Hawley, J. F., & Balbus, S. A. 1991, *ApJ*, 376, 223
Hawley, J. F., & Balbus, S. A. 1992, *ApJ*, 400, 595
Hawley, J. F., Gammie, C. F., Balbus, S. A. 1995, *ApJ*, 440, 742 (HGB95)
Hawley, J. F., Gammie, C. F., Balbus, S. A. 1996, *ApJ*, 464, 690
Hawley, J. F. & Stone, J. M. 1995, *Comput Phys Comm*, 89, 127
Hill, G. W. 1878. *Amer. J. Math.*, 1, 5
Mac Low, M.-M., Norman, M. L., Königl, A., & Wardle, M. 1995, *ApJ*, 442
Matsumoto, R. & Tajima, T 1995, *ApJ*, 445, 767
Ryu, D. & Goodman, J. 1994, *ApJ*, 422, 269
Shakura, N. I., & Sunyaev, R. A. 1973, *A&A*, 24, 337
Stone, J. M. 1997, *ApJ*, 487, 271
Stone, J. M., & Balbus, S. A. 1996, *ApJ*, 464, 364
Stone, J. M., & Norman, M. L. 1992a, *ApJS*, 80, 753
Stone, J. M., & Norman, M. L. 1992b, *ApJS*, 80, 791

Fig. 1.— Numerical growth rates for the radial field in two-dimensional simulations with ionization fraction $f = 0.1$. The solid squares are the 64×64 grid zone simulations (5 cases); the open stars are the 32×32 grid zone simulations (three cases). The solid line is the analytic growth rate from linear stability theory.

Fig. 2.— Time evolution of the individual components of the magnetic energy for the fiducial run Z17 (bold lines) and the high resolution version of the fiducial run (LZ1).

Fig. 3.— Volumetric rendering of (a) the ion density and (b) the magnitude of the toroidal field in the fiducial run at orbit 15. In (a) brightness is a function of density, whereas in (b) the dark regions correspond to strong field. Comparing the two figures shows that the ions lie in thin sheets sandwiched between regions of strong field.

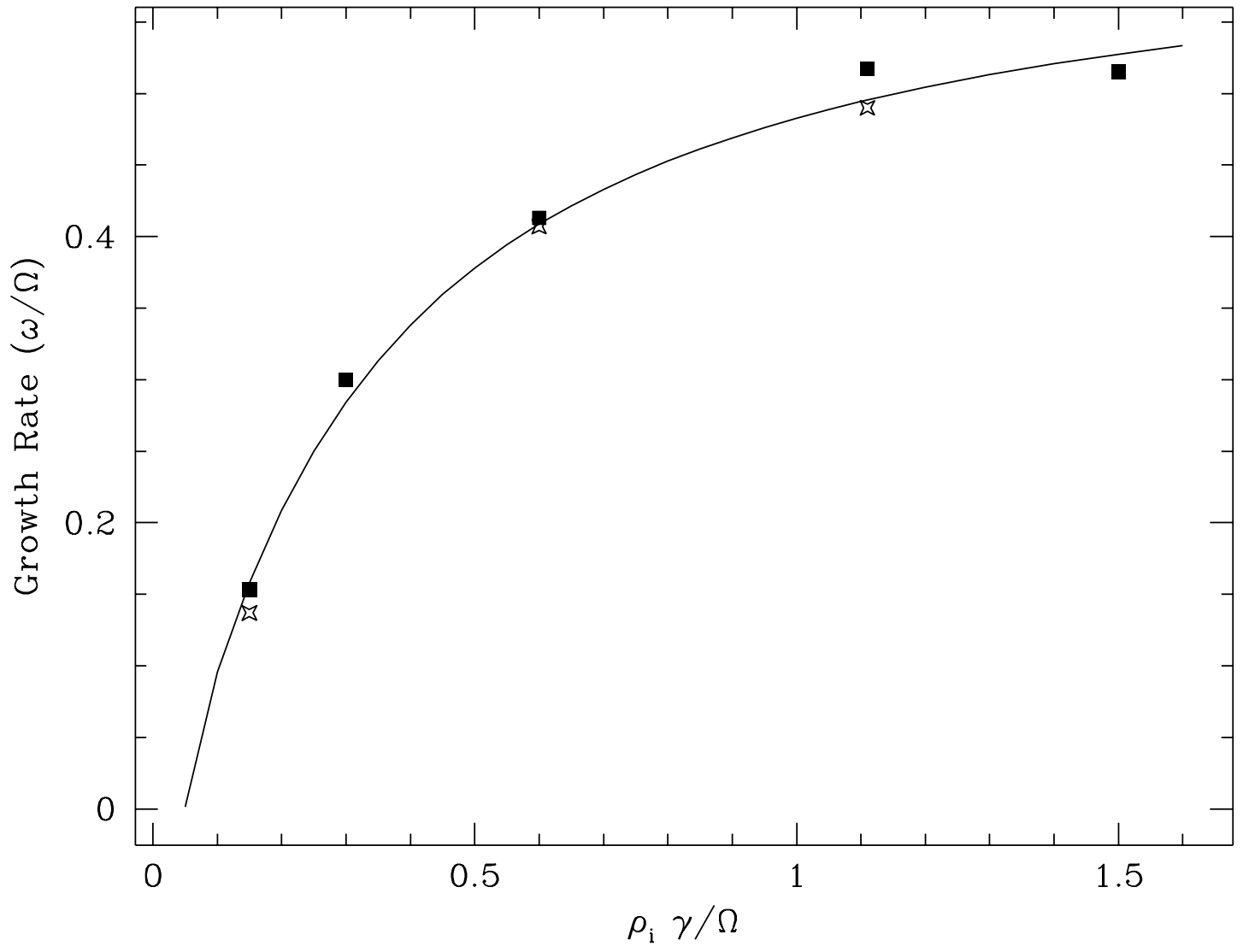
Fig. 4.— Time evolution of the ion and neutral perturbed kinetic energies in the fiducial run (Z17). The behavior of the two curves is very similar; they are offset by the neutral/ion density ratio.

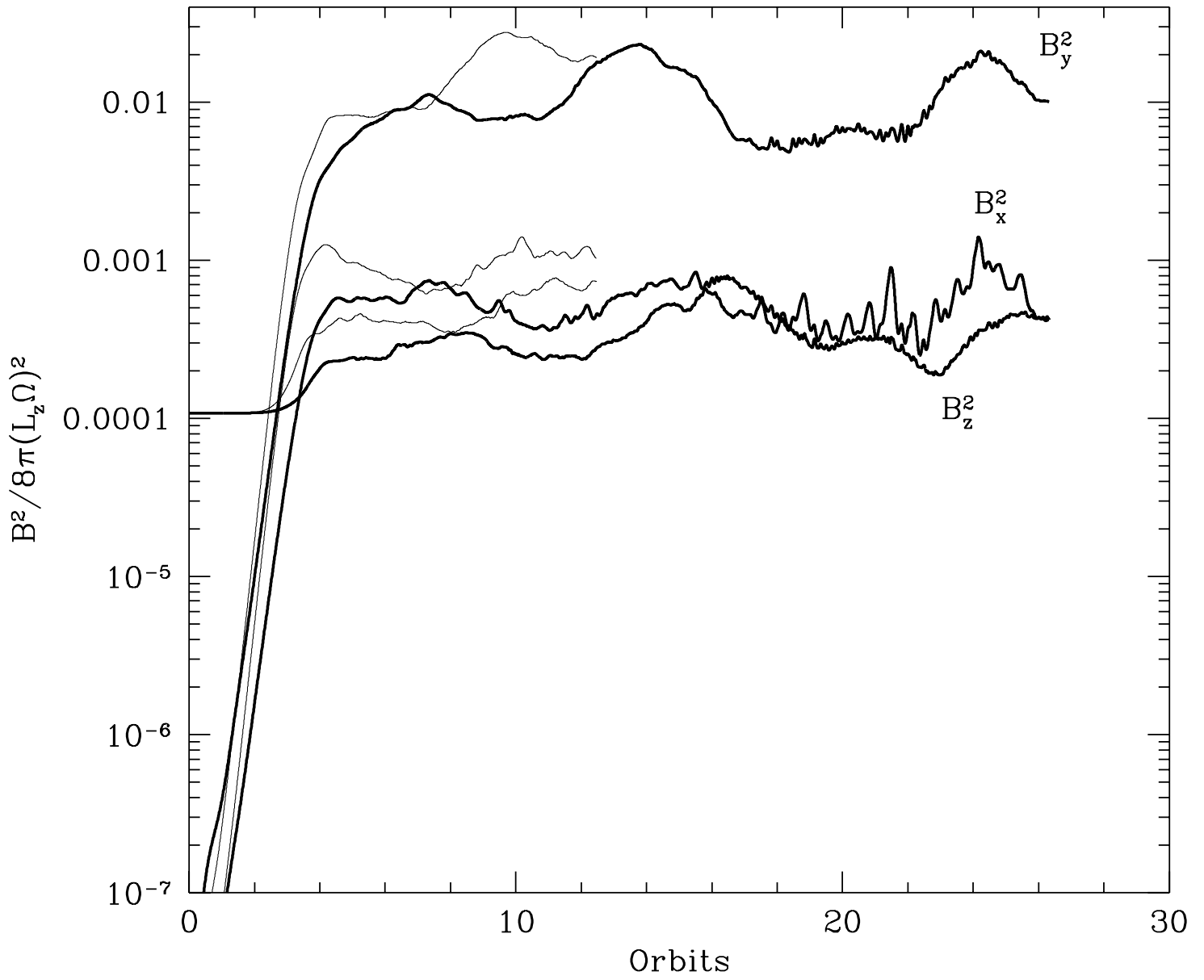
Fig. 5.— Time evolution of the magnetic energy, normalized as the Alfvén speed squared for runs Z17, Z20 and Z21 which have ionization fractions of 0.1, 0.01, and 0.001, respectively. While the total toroidal field amplification is comparable in the three runs, lower ionization fractions produce smaller poloidal field amplification.

Fig. 6.— Time evolution of total magnetic energy for a series of runs with increasing drag coefficient γ . The curves are labeled by their run number, as listed in Table 1. Also included are two single-fluid comparison runs, C1 (with density corresponding to the ion density in the fiducial run) and C2 (with density corresponding to the total density in the fiducial run).

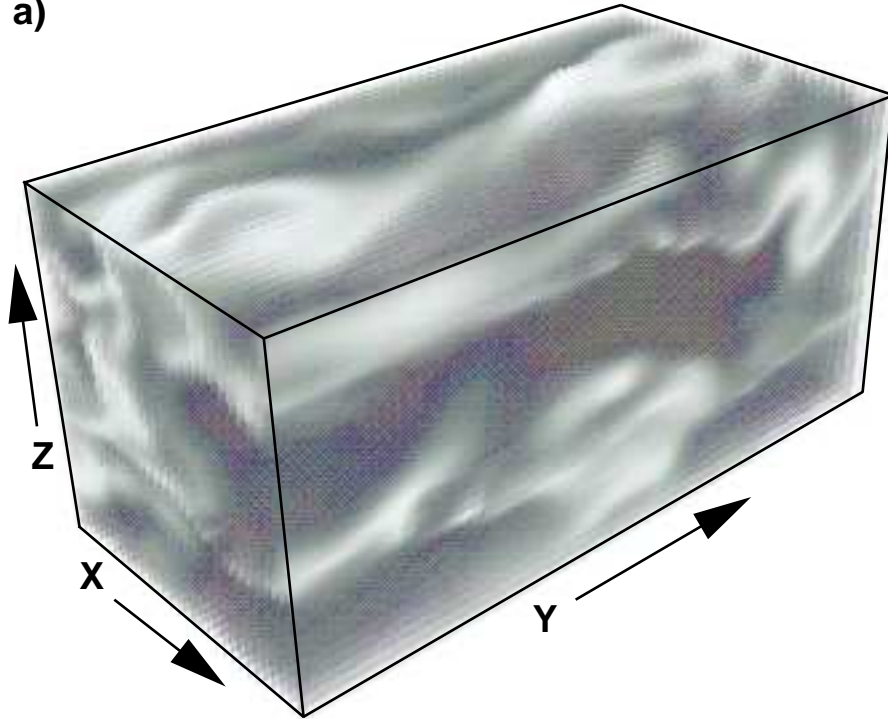
Fig. 7.— Power in fluctuations in v_{zi} (solid) and v_{zn} (dashed) versus wavenumber in the y-direction for the zero net field runs ZN1 (top panel) and ZN2 (bottom panel). The “drag length” is given by eq. (7); $L_{drag} = 0.09L_z$ for the top panel, and $L_{drag} = 0.42L_z$ for the bottom. In ZN2 there is more power at high wavenumbers in the ions than in the neutrals, while in ZN1 they are both comparable. This agrees with the expectation that when the drag length is large (bottom), the ions and neutrals are only weakly coupled, and the ions should show more small scale structure.

Fig. 8.— Time evolution of toroidal (top) and radial (bottom) magnetic field energies in the initial toroidal field runs. The curves are labeled by the run number as listed in Table 4. All show field amplification, although at lower growth rates than the vertical field models.





a)



b)

